Article

Revealing Phase Transition in Ni-Rich Cathodes via a Nondestructive Entropymetry Method

Gulzat Nuroldayeva, Desmond Adair,* Zhumabay Bakenov, and Berik Uzakbaiuly*

Cite This: *ACS Omega* 2023, 8, 37899−37907

Read Online

ACCESS | Metrics & More | Article Recommendations | Supporting Information

ABSTRACT: With the expanding requirements of recent energy regulations and economic interest in high-performance batteries, the need to improve battery energy density and safety has gained prominence. High-energy-density lithium batteries, employed in next-generation energy storage devices, rely on nickel-rich cathode materials. Since they have extremely high charge/discharge capacity, high operating voltage, prolonged cycle life, and lower cost, nickel-rich cathode materials such as Ni-rich NCM ($LiNi_{x > 0.8}Co_yMn_zO_2$) and Ni-rich NCA ($LiNi_{x > 0.8}Co_yAl_zO_2$) are of particular interest to researchers. Several in situ characterization methodologies are currently used to understand lithium-ion battery electrode response and deterioration better. Nevertheless, in many contexts, these measurement methodologies must be combined with specially designed cells and electrode materials with distinct forms, which is sometimes inconvenient. As an alternative, thermo-voltammetric dynamic characterization may be utilized to describe the thermal internal characteristics of various electrode materials, such as the structural changes and electrode reactions that occur during charging and discharging. In this paper, a nondestructive entropy measurement method demonstrates that phase change occurs for NCM ($LiNi_{0.83}Co_{0.12}Mn_{0.05}O_2$) and NCA ($LiNi_{0.88}Co_{0.09}Al_{0.03}O_2$) at 40−30% of state of charge (SOC) and 90−80% of SOC, respectively. This is confirmed by ex situ X-ray diffraction (XRD) measurements for these highly popular cathodes.
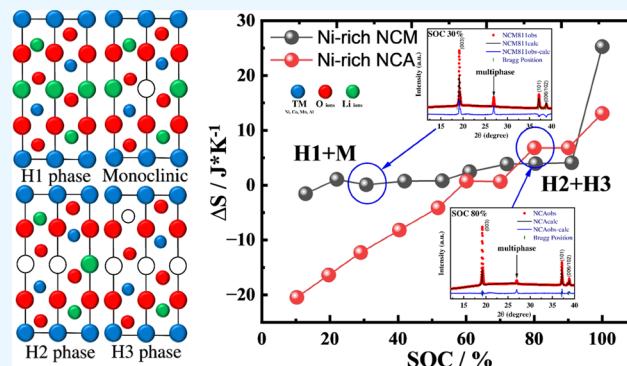
1. INTRODUCTION

With the rising demands of new energy policies and market demand for high-performance batteries, the question of how to enhance the energy density and safety of batteries has gained increasing attention. Nickel-rich cathode materials are vital components of high-energy-density lithium batteries used in next-generation energy storage systems.[1] Due to their high energy density and extended cycle life, lithium-ion batteries (LIBs) increasingly dominate the electronic product industry, such as mobile phones and power tools.[2] LIBs are high-density energy sources for portable electronic devices and small domestic appliances. LIBs, on the other hand, have significant challenges when it comes to replacing gasoline/diesel-powered cars with full-electric vehicles (EVs), which are becoming of increasing importance in establishing a sustainable mode of personal transportation.[3] One of the most challenging technological issues for EV batteries is the increase of their specific energy density, which affects the driving range of EVs per charge. Therefore, high-capacity cathodes for LIBs are emerging as one of the most viable ways for EV batteries.[4] Materials such as nickel-rich ternary cathodes possess relatively high capacity, working voltage, and energy density. At the same time, the costs are relatively low, and $Li(Ni_xCo_yMn_{1−x−y})O2$ (x = 0.6−0.88) is progressively replacing $LiCoO_2$ and other types of cathode materials.[5]

Researchers are particularly interested in nickel-rich cathode materials such as Ni-rich NCM ($LiNi_{0.83}Co_{0.12}Mn_{0.05}O_2$) and Ni-rich NCA ($LiNi_{0.88}Co_{0.09}Al_{0.03}O_2$) because of their high charge/discharge capacity, high operating voltage, extended cycle life, and low cost.[6] However, numerous disadvantages prevent their extensive use in LIBs compared to lower-Ni-concentration materials.[7] One of the challenges is the unstable oxygen element: the oxygen in the layered structure of Ni-rich NCM and NCA is easily displaced during cycling or at high temperatures, resulting in oxygen flaws from lattice faults. This poses a safety risk. Hence, the hoped-for widespread usage of lithium-ion batteries with high-nickel-content cathode materials is still underway.[8] The specific capacity of Ni-rich cathode materials may approach 220 mAh/g (Ni > 0.80−0.88 mol %) as the nickel concentration increases, resulting in an energy density of 300 Wh/kg for a single cell.[9] Although potassium-ion and lithium−sulfur batteries are being explored as

alternatives to high-energy-density batteries, high-nickel-content NCA/NCM for lithium-ion batteries is currently the sole material that can be utilized commercially. The advantages of their constituent elements are combined in these oxides: nickel boosts capacity, cobalt lowers cationic mixing while boosting rate capability, and manganese stabilizes the structure and improves the thermal stability.[10]

A detailed overview of the heat-generating characteristics of cells during both charging and discharging, which would be influenced by the properties of the electrode material itself, is required for design improvement.[11] Many in situ characterization approaches are now being employed to better understand the electrode response and degradation process of lithium-ion batteries.[12] However, in many circumstances, these characterization approaches must be paired with specifically constructed cells and electrode materials with unique shapes, which is sometimes inconvenient. As an alternative, direct measurement of the thermodynamic data of the electrode response is a viable and cost-effective method of electrode characterization that material researchers frequently overlook. Furthermore, thermodynamic characterization may describe the thermal characteristics of various electrode materials and the structural changes and electrode reactions that occur during charging and discharging.[13] It is a practical approach for investigating battery cycle life and safety.[14]

Gibbs free energy G, entropy S, and enthalpy H are the electrode reaction's three essential thermodynamic parameters.[15] The maximal work of the battery is the change in Gibbs free energy ΔG. The shift in entropy ΔS characterizes the change in the lattice order. The reaction heat of the electrochemical process is represented by the enthalpy change ΔH. These three factors can be assessed using electrochemical testing with the calculations below[15]

$$\Delta G = -nFE \tag{1}$$

$$\Delta S = nF\left(\frac{\partial E}{\partial T}\right)_P \tag{2}$$

$$\Delta H = \Delta G + T\Delta S = nF\left[\left(\frac{\partial E}{\partial T}\right)_P - E\right] \tag{3}$$

where n is the number of electrons, F represents the Faraday constant, E represents the standard electromotive force [also known as the open-circuit potential (OCV)] of the battery reaction, T represents the temperature, and P represents the pressure. The term $(\partial E/\partial T)_P$ is calculated by measuring the OCV of the electrochemical cell at various temperatures.[16] To achieve equilibrium, the cell should be relaxed for a period of time before measuring the open-circuit voltage. The increase or drop in entropy corresponds to the decrease or increase in the number of lithium ions in the cathode matrix. More significantly, changes in entropy can alter the thermal performance of electrochemical processes, so changing the temperature of the battery significantly influences the efficiency of lithium-ion batteries.[17] According to eq 2, ΔS is a process-independent state function, meaning that it is unaffected by the charging and discharging processes and solely varies with the concentrations of the lithium ion. The entropy state variable can express the link between entities.[18] The entropy change characterization for cathode materials, such as lithium nickel cobalt manganese oxide (NCM) and lithium nickel cobalt

aluminum oxide (NCA), typically involves understanding the changes in the lattice structure and their effects on thermodynamic properties.[19,20]

The main reasons for lattice change in the structure of cathode materials can include the following:

1. Lithium-ion intercalation/deintercalation: The process of discharging involves the insertion of lithium ions (Li^+) into the crystal lattice of the cathode material, while charging causes their removal through deintercalation. This process causes changes in the spacing between lattice planes and leads to structural expansion or contraction, resulting in changes in the entropy of the material.[21]

2. Redox reactions: Cathode materials in lithium-ion batteries typically undergo redox reactions, where transition metal ions (e.g., Ni, Co, Mn, Al) change their oxidation states. This redox reaction can induce changes in the crystal structure and lattice parameters, leading to changes in the entropy of the material.[22]

3. Phase transitions: Cathode materials can undergo phase transitions, such as from a layered structure to a spinel structure or vice versa, during battery operation. These phase transitions can result in changes in the entropy of the material as the arrangement of atoms and ions in the crystal lattice changes.[23]

4. Defect formation/annihilation: Defects, such as vacancies or interstitials, can form or annihilate in the crystal lattice of cathode materials during battery operation. These defects can affect the entropy of the material by changing the arrangement and mobility of atoms or ions in the lattice.[24]

5. Structural disorder/order: Changes in the structural disorder/order of the cathode material can also lead to changes in entropy. For example, the disorder of transition metal cations in the cathode material's crystal structure can increase during charging and decrease during discharging, affecting the entropy of the material.[25]

Understanding these lattice changes and their effects on the entropy of cathode materials is crucial for optimizing the performance and stability of lithium-ion batteries, as they can impact their thermodynamic properties, such as capacity, voltage, and cycling stability.[26]

Anyone can develop more accurate thermoelectric-coupled modeling using these fundamental physical chemistry factors, allowing them to accurately forecast and simulate rechargeable batteries' electrochemical and thermodynamic properties.[27,28] In this paper, we investigated the entropy profiles of Ni-rich NCM ($LiNi_{0.83}Co_{0.12}Mn_{0.05}O_2$) and NCA ($LiNi_{0.88}Co_{0.09}Al_{0.03}O_2$) at different states of charge (SOC) of the cathodes. Entropy measurements revealed a phase transition region corroborated with the X-ray diffraction (XRD) measurement results confirming the approach developed in this work.

2. EXPERIMENTAL SECTION

2.1. Electrochemical Testing. The commercial powders of $LiNi_{0.83}Co_{0.12}Mn_{0.05}O_2$ and $LiNi_{0.88}Co_{0.09}Al_{0.03}O_2$ (Xiamen Tob New Energy Technology Co., Ltd), PVDF (poly-(vinylidene fluoride), Arkema HSV900), and conductive carbon black (Super P and KS-6, TIMCAL Graphite) in a weight ratio of 80:10:10 were thoroughly mixed in the NMP

solvent (*N*-Methyl-2-pyrrolidone, Sigma-Aldrich), doctor-bladed on an aluminum foil current collector, predried at 60 °C, and moved to a vacuum oven to dry for 4 h at 60 °C. The dried cathode parts were punched into 14 mm diameter circles, and 2032 coin-type half-cells were assembled with these cathodes in an argon-filled glovebox (Labmaster, MBRAUN Inc.) using 1 M $LiPF_6$ in 1:1 in a mixture of ethylene carbonate and diethyl carbonate (EC/DEC, 50/50 v/v %) as the electrolyte, Celgard 2203 as the separator, and lithium metal (AME-Energy) as a counterpart electrode. The cells were charged and discharged at 25 °C between 2.7 and 4.3 V at a constant current density of 180 mAh g^{-1} (0.1C rate) using multichannel battery testers (Arbin Instruments BT-I), Neware BTS 4000 in a temperature controller chamber (LIB Industry). All potentials are given vs the lithium metal electrode.

2.2. Physicochemical Characteristics. X-ray diffraction (XRD) patterns of the powder samples were obtained by a Rigaku MiniFlex 600 X-ray diffractometer. At room temperature, a six-multi-detector system was used to capture XRD data throughout in the range 10–80° 2θ with a 0.02° step width. For ex situ XRD measurements, the cells were disassembled in a glovebox, the cathodes were washed with the DEC solvent, dried in an Ar-filled glovebox, and immediately transferred for XRD measurements. The structural refinement was carried out using the Rietveld analysis and the Fullprof suite. Scanning electron microscopy (SEM) was used to examine the morphologies and structures of the prepared samples (ZEISS Crossbeam 540). The chemical compositions of the commercial powders were determined using inductively coupled plasma optical emission spectroscopy (ICP-OES) (Thermo Fisher Scientific iCAP 6300 DUO). A NEXSA (Thermo Scientific) X-ray photoelectron spectrometer (XPS) was used to determine the oxidation state and bond information of the samples.

2.3. Entropy Measurements. The coin cells were first charged to 4.3 V and discharged to 2.7 V at a 0.1C rate in order to determine incremental capacity. The cells were charged again and left for 24 h to achieve the equilibrium state. The open-circuit voltage (OCV) test was measured at 25, 20, 15, 10, and 20 °C for 2 h at the first temperature step and 1 h at each remaining step. OCV was monitored at each SOC while the temperature was varied. For the temperature variation, the temperature-controlled chamber temperature was first maintained at 25 °C for 120 min, then lowered to 20 °C for 60 min, and so on for all temperatures for cell tests at a 0.1C rate. The OCV profile was corrected for accurate entropy measurement by linearly fitting the baseline between the OCV parameters determined at the first 20 °C and the recovered 20 °C.

All calculations were done using the MATLAB Simulink program. First, the experimental SOC was calculated using Coulomb's method and compared with computed SOC for all SOC of coin cells using the Faraday constant and practical OCV. Following that, using eq 1, the Δ*G* was calculated, where the number of transferred electrons was directly proportional to the OCV. All of the obtained data was utilized to construct the slope of OCV *vs.* temperature using linear regression in the MATLAB Simulink program.

3. RESULTS AND DISCUSSION

3.1. SEM/EDS Analysis. SEM images were taken to observe the morphologies and structures of the commercial particles. The images (Figure 1) demonstrate that the cathode
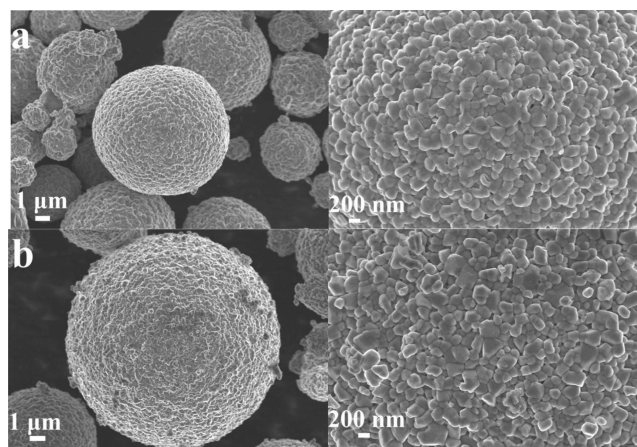

Figure 1. SEM images of (a) Ni-rich NCM and (b) Ni-rich NCA.

particles for each composition were comparable in size (4–25 *μ*m in diameter) and shape. Furthermore, each secondary particle comprised nanosized primary particles (200–400 nm wide) firmly packed. Additional focusing revealed that each secondary particle was comprised of highly agglomerated parent particles.

The energy-dispersive spectroscopy (EDS) mapping analysis shows the uniform distribution of Ni, Co, and Mn, Al in the NCM microsphere (Figure S1, Supporting information). All of the above indicates that the different morphological and structural features of LIBs are favorable for the electrochemical performance improvement. The chemical compositions of the powders were determined using an inductively coupled plasma optical emission spectrometry (ICP-OES). The LIB material shows molar ratios of Ni, Co, Al, Mn, and Li, corresponding to the formula $LiNi_{0.83}Co_{0.12}Mn_{0.05}O_2$ and $LiNi_{0.88}Co_{0.09}Al_{0.03}O_2$ (Tables S1 and S2 in the Supporting Information). Both of the cathodes demonstrate a high Ni content.

3.2. XRD Analysis. For detailed structural analysis, XRD patterns of the as-synthesized powder samples were obtained (Figure S2, Supporting information). The XRD patterns prove that they lack impurity phases and consist of a hexagonal a-$NaFeO_2$-type structure with an *R3m* space group. In the XRD spectra of all of the powders, significant peak splits corresponding to Miller indices of (006)/(102) and (018)/(110) for NCM and (006)/(102) and (108)/(110) for NCA reveal the formation of layered structures in both cases.[6] The I_{003}/I_{104} = 1,41 (NCM) and I_{003}/I_{104} = 1,48 (NCA) mean less cation mixing in the structure.[1] Ni-rich NCM and NCA materials have substantial cation mixing, structural disintegration, and capacity fading. In general, cation mixing occurs during the material synthesis as a result of Li/Ni site exchange due to the similar radii of Li^+ (0.076 nm) and Ni^{2+} (0.069 nm), and the decomposition reaction is accompanied by the oxygen release, which is dangerous due to its reaction with organic electrolyte.

3.3. XPS Analysis. XPS measurements were performed to explore the specific composition and chemical behavior of the cathodes $LiNi_{0.83}Co_{0.12}Mn_{0.05}O_2$ and $LiNi_{0.88}Co_{0.09}Al_{0.03}O_2$ and also to understand the NCM and NCA cathode surface elements. As shown in Figure 4, for NCM, three peaks were identified in the C 1s spectrum: 284.58 eV (C–C), 286.38 eV (C=O), and 291.18 eV (C–F). These peaks are derived from Super P, PVDF, and electrolyte decomposition products. For the O 1s spectrum, C=O (532.48 eV) peaks were also found
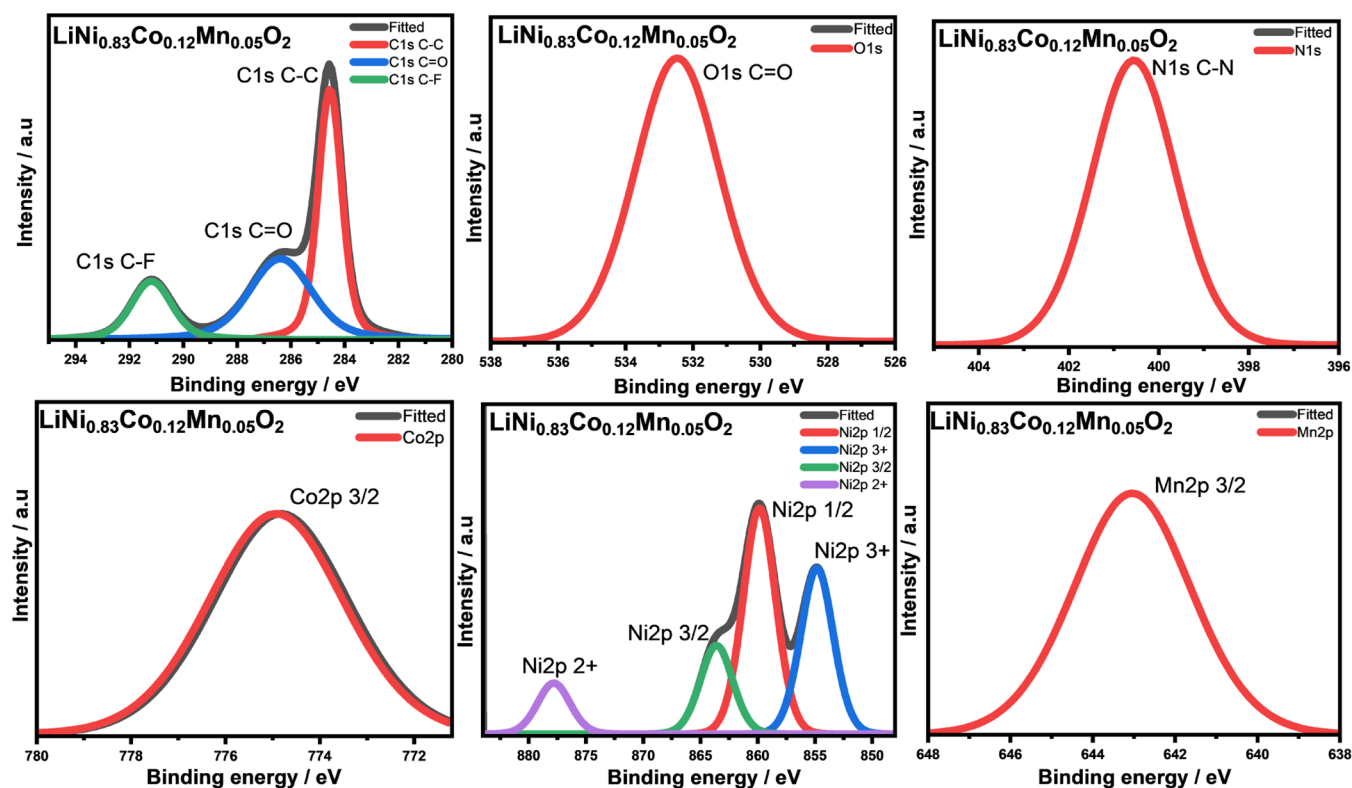
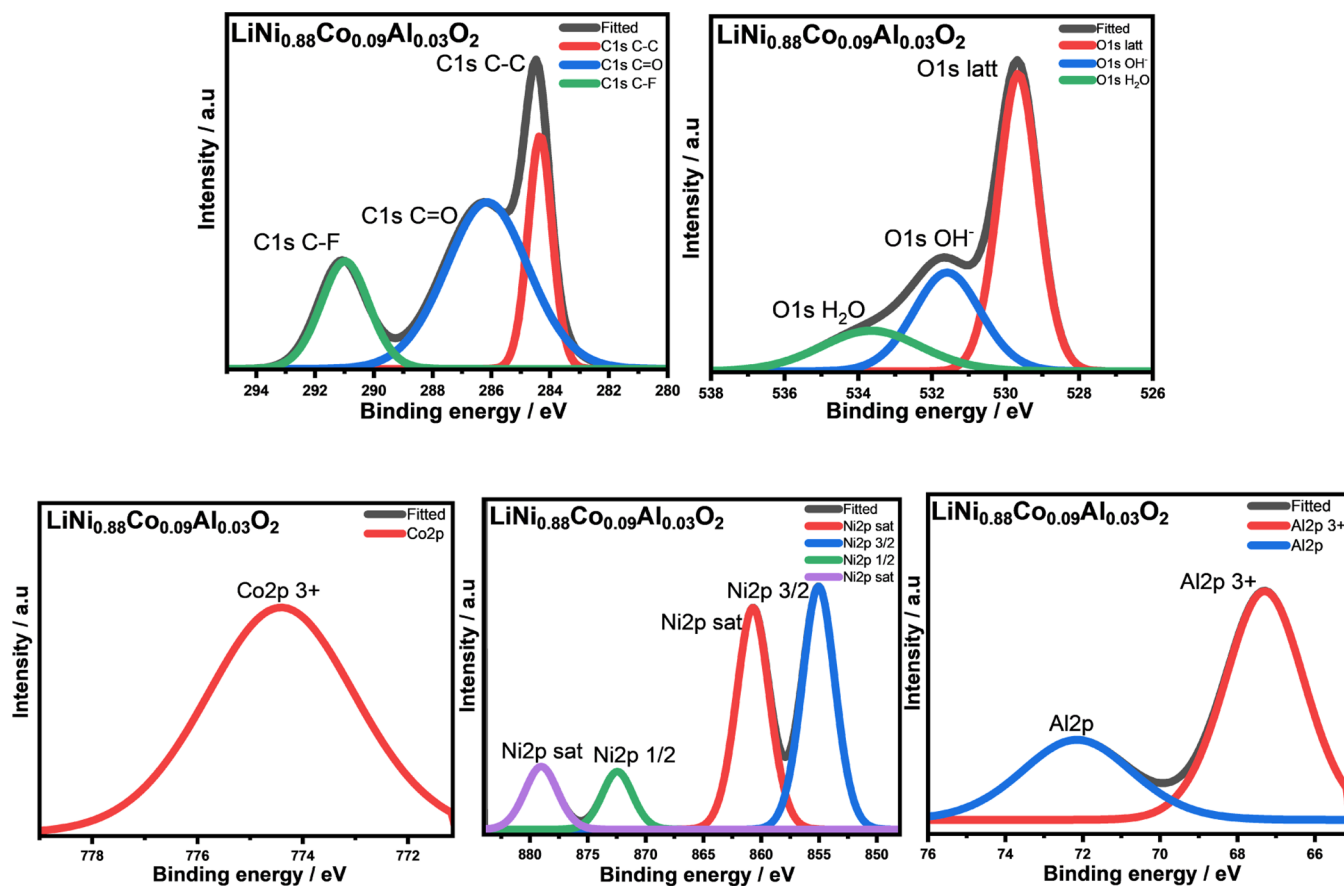**Figure 2.** XPS analysis of the Ni-rich NCM cathode material.

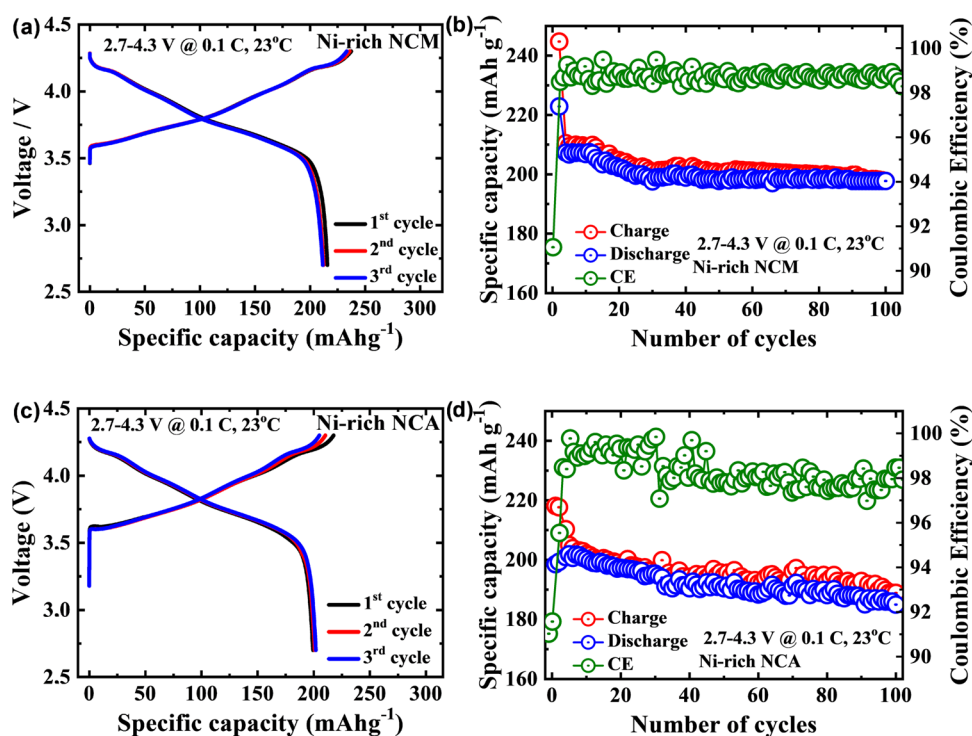**Figure 3.** XPS analysis of the Ni-rich NCA cathode material.

Figure 4. Potential profiles and cycling performance of (a, b) Ni-rich NCM and (c, d) Ni-rich NCA cathodes, respectively.
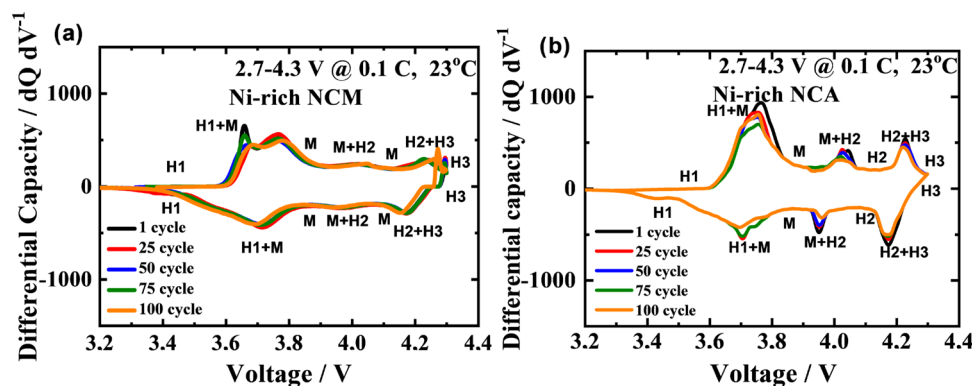

Figure 5. Differential Capacity (dQ/dV) profiles of (a) Ni-rich NCM and (b) Ni-rich NCA cathodes.

as shown in Figure 2. For the N 1s spectrum, the C−N peak (400.58 eV) is only found again as shown in Figure 2.

Figure 3 shows the Ni 2p, Co 2p, and Mn 2p spectra of cycled Ni-rich NCA cathodes after 50 cycles. Two strong satellites (labeled as "sat") near two spin−orbit doublets at 872.48 and 860.68 eV (the spin-energy separation is 11.8 eV) may be distinguished as Ni 2p1/2 and Ni 2p3/2 signals of Ni^{2+} in the high-resolution XPS pattern of NCA Ni 2p. Moreover, strong satellite peaks imply that the bulk of the nickel element in the lattice structure is Ni 2p cations.[29] The Co 2p XPS spectrum likewise divides into two spin−orbit doublets, demonstrating the existence of high-spin Co^{3+}. The peak is at 774.38 eV, and the intensity of the Co 2p3/2 satellite line is relatively modest. The O 1s spectrum has three distinct peaks: H_2O, OH, and lattice oxygen.[30]

The XPS results demonstrate that this material has redox states of Co and Ni, contributing significantly to both pseudo-capacitance and high conductivity in the electrochemical processes.

3.4. Electrochemical Performance. The potential profiles and cycling performance of Ni-rich NCM and Ni-rich NCA cathodes are summarized in Figure 4. The initial cycle charge−discharge curves at 0.1C reveal that as the concentration of active redox Ni ions rose, the discharge capacity increased: $LiNi_{0.83}Co_{0.12}Mn_{0.05}O_2$—222.86 mAh/g (Figure 4a) and $LiNi_{0.88}Co_{0.09}Al_{0.03}O_2$—198.56 mAh/g (Figure 4c). The cathodes functioned well upon prolonged cycling, and the discharge capacity remained relatively stable for 100 cycles.

The differential capacity (dQ/dV) profiles generated by differentiating the 1st, 25th, 50th, 75th, and 100th charge/discharge cycles at 23 °C are shown in Figure 5. It depicts the structural changes of the cathodes throughout cycling (Figure 5a,b). Three oxidation peaks were detected in the dQ/dV curves for conventional Ni-rich NCA and Ni-rich NCM, identical to that of the $LiNiO_2$ cathode. The oxidation peaks correspond to the phase transitions of H1 to M (original hexagonal to monoclinic), M to H2 (monoclinic to hexagonal), and H2 to H3 (hexagonal to hexagonal). The shift from H2 to H3 at 4.15−4.2 V implies a negative lattice
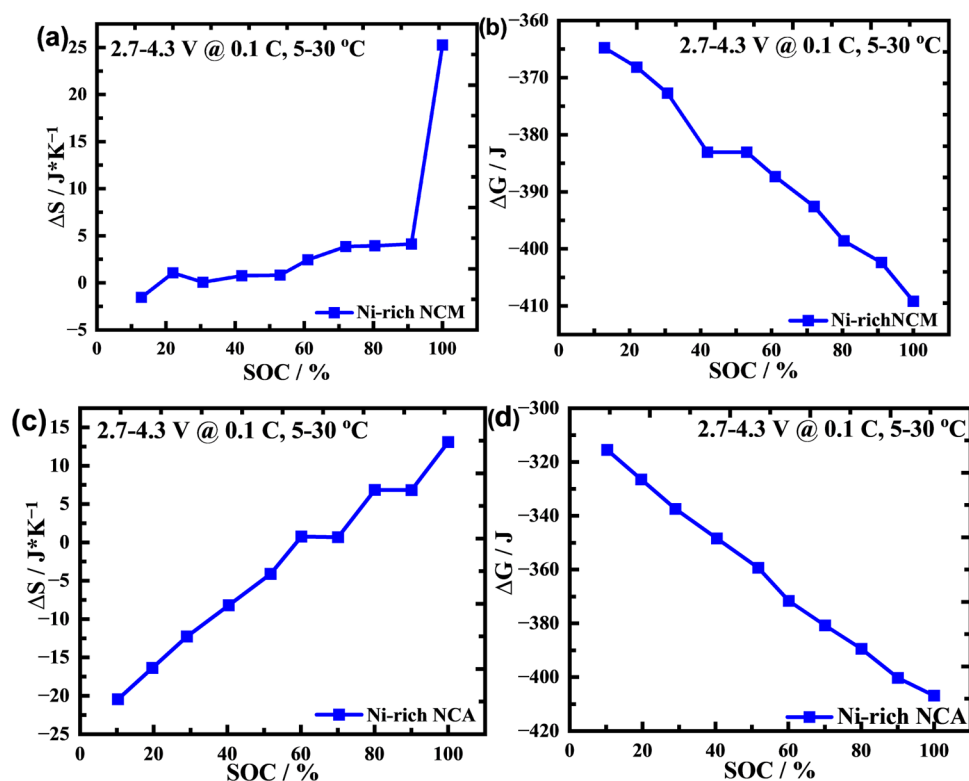
Figure 6. ΔS and ΔG vs SOC profile of (a, b) Ni-rich NCM and (c, d) Ni-rich NCA cathodes, respectively.
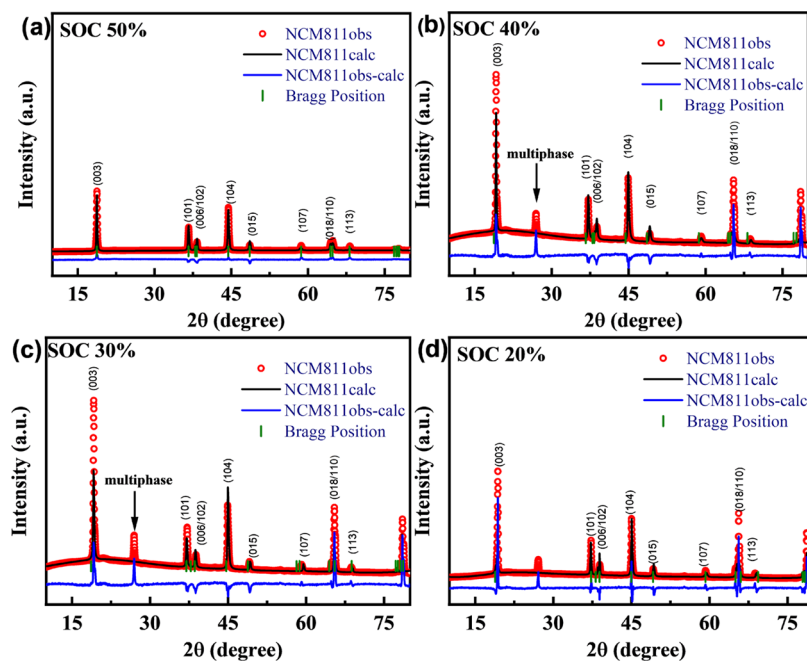

Figure 7. Ex situ XRD analysis of Ni-rich (a) SOC 50% (NCM), (b) SOC 40% (NCM), (c) SOC 30% (NCM), and (d) SOC 20% (NCM).

shrinkage in the c-direction, followed by mechanical strain in the material, lowering its cycle performance. The intensity of the conventional Ni-rich NCA and Ni-rich NCM's H2 to H3 peaks reduced dramatically, suggesting that the cathode material suffered a significant structural change during the charge/discharge cycles. The structural change is generally related to the phase shift generated by the cathode material and electrolyte side reactions.[1]

The movement of the phase transition peaks of the H2 to H3 toward lower potentials also suggests irreversible structural change, which is generally accompanied by structural collapse due to mechanical strain. The anisotropic volume change of the material during charge/discharge cycles causes mechanical strain to aggregate, causing secondary particles to shatter along micropores and grain boundaries.[31] Secondary particle cracking causes other side reactions and reduces the cycling performance of active materials, which is consistent with the
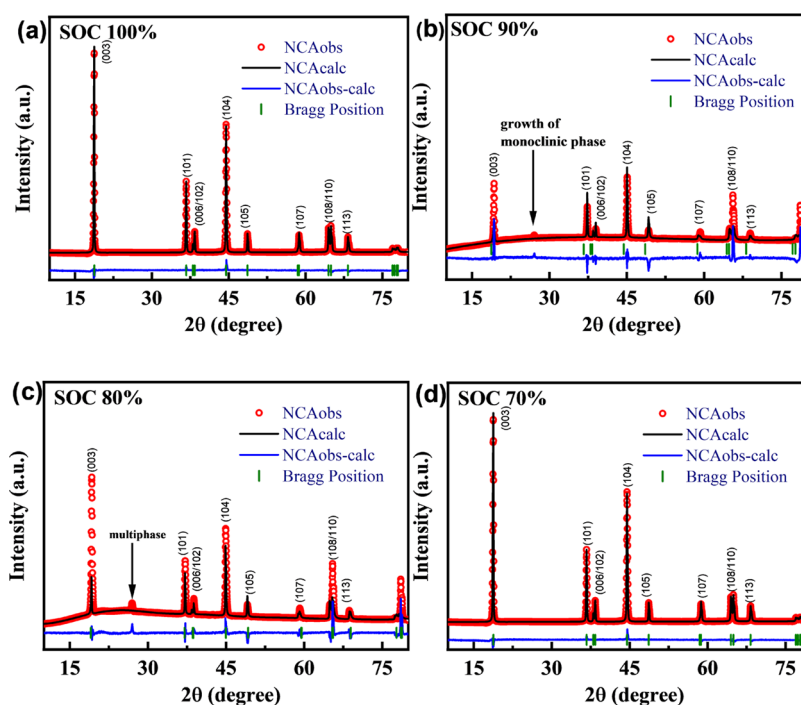
Figure 8. Ex situ XRD analysis of Ni-rich (a) SOC 100% (NCA), (b) SOC 90% (NCA), (c) SOC 80% (NCA), and (d) SOC 70% (NCA).

dQ/dV profiles and cycling data. The pressure created by repeated charging and discharging was absorbed by opening and closing the particle boundaries without permanently damaging the secondary particles.

3.5. Entropy Measurement. The helpful and straightforward approach for evaluating the entropy value as a function of SOC was devised in this work under the same atmospheric conditions as the typical battery operating state. As noted in the Introduction section, entropy was calculated using the Gibb's free energy connection and the Nernst equation. According to the results, OCVs change significantly over the battery's life at specific temperatures. The most significant change is observed between 10 and 20 °C. A more detailed study of the effect of LIB aging found that the difference between the measured OCVs after discharge changes significantly over the battery's life. The pattern for Ni-rich NCM is that when the temperature rises, the sample's OCV rises (Figure 6). A phase transition is detected between SOC = 40−30% for Ni-rich NCM because ΔS displays a change in the slope sign in those ranges (Figures 6a and S3). This indicates that the reaction in this region is in a transition state, which is a multiphase coexistence region for Ni-rich NCM. The same pattern appears for Ni-rich NCA between SOC of 90−80% (Figures 6c and S4). Therefore, these regions correlate to the $Mn^{4+} \rightarrow Mn^{3+}$ redox couple rather than the $Ni^{2+} \rightarrow Ni^{3+} \rightarrow Ni^{4+}$ redox couple. In addition, the lithium intercalation reaction has been described as a two-phase reaction.[13,32] ΔS also does not change the sign in the 100−60% SOC range for NCM and 70−10% SOC range for NCA materials, showing that these regions are closer to the reaction mechanism for a single-phase system.

3.6. Ex Situ XRD Analysis. From the ex situ XRD analysis for the SOC 50%, SOC 40%, SOC 30%, and SOC 20% of NCM, one peak was observed in the region of 27° (Figure 7a−d). The observed peak grows at SOC 40% and diminishes at SOC 20% for NCM. This additional peak is related to a

multiphase coexistence in the lattice structure. Except for the less-intense additional peaks at lower 2θ angles (indicated by a dotted square), all of the primary peaks in the pristine NMC and NCA powders (Figure S2a,b) may be attributed to the rhombohedral or trigonal ($R\overline{3}m$ space group, represented as O_3) phase. In accordance with earlier publications, these (additional) reflections in the XRD pattern from the Ni-rich NMC and Ni-rich NCA materials suggest cation ordering between lithium and TM ions in the TM layers and confirm the presence of Li_2MnO_3-like areas.[33−35]

Ex situ XRD examination of NCA SOC 100%−SOC 70% revealed one peak in the area of 27°. The observed peak grows at SOC 90% and decreases at SOC 70% (Figure 8a−d). These (extra) reflections in the XRD pattern from the Ni-rich NMC and Ni-rich NCA materials show cation ordering between lithium and TM ions, which is consistent with a previous report, and they are consistent with the entropy measurements above.[36]

Most crucially, when the dQ/dV vs V peaks for NCM 3.5 V and NCA 4.17 V (vs Li/Li⁺) demonstrate kinetic obstruction due to poor lithium diffusion and are partially or entirely avoided during charge−discharge cycling, the positive electrode active mass loss can be reduced.[37] Therefore, the existence of multiphase is observed in the region of 3.5 V, which corresponds to SOC 40−30% for NCM cathodes, and 4.17 V, which corresponds to SOC 90−80% for NCA active materials. Since lithium diffusion is sluggish, more large lithium concentration gradients arise in particles, and because lattice constants vary with lithium content, internal strains and stress increase. If particle fracture is to be avoided, avoiding regions of sluggish Li-ion diffusion is critical. This can also be confirmed by entropy measurements in Figure 6a,c. As shown in Figure. S3, NCM has a change in slope in the 40−30% SOC region, corresponding to the multiphase transition region. This is in contrast to the NCA, which has a multiphase transition region of around the 90−80% SOC. In fact, when the NCA

material is not fully charged, better performance is reported (Figure S4).[37]

4. CONCLUSIONS

It was discovered that the entropy and enthalpy profiles change considerably depending on the OCV used. As revealed by post-mortem X-ray diffractometry, these alterations correspond well with the cathode crystal structure deterioration. By including the temperature parameter in our analysis, we can separate the free energy into its two components, enthalpy and entropy, and get further insights into the electrode thermodynamics that isotherm studies do not allow for. Using this nondestructive method, it was revealed there was a multiphase coexistence in 30% of the SOC region for NMC and 80% of the SOC region for NCA. Thus, information about cathodes can be found without opening up the cell. It may be that more accurate thermodynamic-coupled modeling to achieve accurate prediction and simulation of lithium-ion battery electrochemical performance and thermal behavior is possible.

■ ASSOCIATED CONTENT

Ⓢ Supporting Information

The Supporting Information is available free of charge at https://pubs.acs.org/doi/10.1021/acsomega.3c03245.

> EDS mapping analysis; ICP-OES results; ex situ XRD analysis (Rietveld Refinement) at SOC 100−10%; OCV vs temperature profile of Ni-rich NCM and NCA; thermodynamic characteristics; and EIS profile (PDF)

■ AUTHOR INFORMATION

Corresponding Authors

Desmond Adair − *Institute of Batteries LLC, Astana 010000, Kazakhstan; Department of Mechanical and Aerospace Engineering, Nazarbayev University, Astana 010000, Kazakhstan;* Email: dadair@nu.edu.kz

Berik Uzakbaiuly − *Institute of Batteries LLC, Astana 010000, Kazakhstan; Department of Chemical and Materials Engineering, Nazarbayev University, Astana 010000, Kazakhstan; National Laboratory Astana, Astana 010000, Kazakhstan;* ⓘ orcid.org/0000-0002-0964-0392; Email: berik.uzakbaiuly@nu.edu.kz

Authors

Gulzat Nuroldayeva − *Institute of Batteries LLC, Astana 010000, Kazakhstan; Department of Chemical and Materials Engineering, Nazarbayev University, Astana 010000, Kazakhstan*

Zhumabay Bakenov − *Institute of Batteries LLC, Astana 010000, Kazakhstan; Department of Chemical and Materials Engineering, Nazarbayev University, Astana 010000, Kazakhstan; National Laboratory Astana, Astana 010000, Kazakhstan;* ⓘ orcid.org/0000-0003-2781-4955

Complete contact information is available at:
https://pubs.acs.org/10.1021/acsomega.3c03245

Notes

The authors declare no competing financial interest.

■ ACKNOWLEDGMENTS

■ ABBREVIATIONS

SOC, state of charge; LIB, lithium-ion batteries; EV, electric vehicle; XRD, X-ray diffraction; BTS, battery testing system; ICP-OES, inductively coupled plasma optical emission spectrometry; XPS, X-ray photoelectron spectrometer; EDS, energy-dispersive spectroscopy; SEM, scanning electron microscopy

■ REFERENCES

(1) Wan, S.; Chen, S. A Dithiol-Based New Electrolyte Additive for Improving Electrochemical Performance of NCM811 Lithium Ion Batteries. *Ionics* **2020**, *26*, 6023−6033.

(2) Li, J.; Li, Y.; Yi, W.; Ma, P. Improved Electrochemical Performance of Cathode Material LiNi0.8Co0.1Mn0.1O2 by Doping Magnesium via Co-Precipitation Method. *J. Mater. Sci.: Mater. Electron.* **2019**, *30*, 7490−7496.

(3) Ryu, H.-H.; Park, K.-J.; Yoon, C. S.; Sun, Y.-K. Capacity Fading of Ni-Rich Li[Ni$_x$ Co$_y$ Mn$_{1−x−y}$]O$_2$ ($0.6 \leq x \leq 0.95$) Cathodes for High-Energy-Density Lithium-Ion Batteries: Bulk or Surface Degradation? *Chem. Mater.* **2018**, *30*, 1155−1163.

(4) Atar, N.; Eren, T.; Yola, M. L. Ultrahigh Capacity Anode Material for Lithium Ion Battery Based on Rod Gold Nanoparticles Decorated Reduced Graphene Oxide. *Thin Solid Films* **2015**, *590*, 156−162.

(5) Zhang, C.; Qi, J.; Zhao, H.; Hou, H.; Deng, B.; Tao, S.; Su, X.; Wang, Z.; Qian, B.; Chu, W. Facile Synthesis Silkworm-like Ni-Rich Layered LiNi0.8Co0.1Mn0.1O2 Cathode Material for Lithium-Ion Batteries. *Mater. Lett.* **2017**, *201*, 1−4.

(6) Noh, H.-J.; Youn, S.; Yoon, C. S.; Sun, Y.-K. Comparison of the Structural and Electrochemical Properties of Layered Li-[NixCoyMnz]O2 ($x = 1/3$, 0.5, 0.6, 0.7, 0.8 and 0.85) Cathode Material for Lithium-Ion Batteries. *J. Power Sources* **2013**, *233*, 121−130.

(7) Ryu, H.-H.; Park, N.-Y.; Noh, T.-C.; Kang, G.-C.; Maglia, F.; Kim, S.-J.; Yoon, C. S.; Sun, Y.-K. Microstrain Alleviation in High-Energy Ni-Rich NCMA Cathode for Long Battery Life. *ACS Energy Lett.* **2021**, *6*, 216−223.

(8) Zhang, H.; Yang, S.; Huang, Y.; Hou, X. Synthesis of Non-Spherical LiNi$_{0.88}$ Co$_{0.09}$ Al$_{0.03}$ O$_2$ Cathode Material for Lithium-Ion Batteries. *Energy Fuels* **2020**, *34*, 9002−9010.

(9) Park, K.-J.; Choi, M.-J.; Maglia, F.; Kim, S.-J.; Kim, K.-H.; Yoon, C. S.; Sun, Y.-K. High-Capacity Concentration Gradient Li[Ni$_{0.865}$ Co$_{0.120}$ Al$_{0.015}$]O$_2$ Cathode for Lithium-Ion Batteries. *Adv. Energy Mater.* **2018**, *8*, No. 1703612.

(10) Liu, W.; Oh, P.; Liu, X.; Lee, M.-J.; Cho, W.; Chae, S.; Kim, Y.; Cho, J. Nickel-Rich Layered Lithium Transition-Metal Oxide for High-Energy Lithium-Ion Batteries. *Angew. Chem., Int. Ed.* **2015**, *54*, 4440−4457.

(11) Liu, K.; Liu, Y.; Lin, D.; Pei, A.; Cui, Y. Materials for Lithium-Ion Battery Safety. *Sci. Adv.* **2018**, *4*, No. eaas9820.

(12) Ramdon, S.; Bhushan, B.; Nagpure, S. C. In Situ Electrochemical Studies of Lithium-Ion Battery Cathodes Using Atomic Force Microscopy. *J. Power Sources* **2014**, *249*, 373−384.

(13) Yazami, R.; Reynier, Y.; Fultz, B. Entropymetry of Lithium Intercalation in Spinel Manganese Oxide: Effect of Lithium Stoichiometry. *ECS Trans.* **2006**, *1*, 87−96.

(14) Deng, J.; Bae, C.; Marcicki, J.; Masias, A.; Miller, T. Safety Modelling and Testing of Lithium-Ion Batteries in Electrified Vehicles. *Nat. Energy* **2018**, *3*, 261−266.

(15) Mao, J.; Zhang, P.; Liu, X.; Liu, Y.; Shao, G.; Dai, K. Entropy Change Characteristics of the LiNi$_{0.5}$ Mn$_{1.5}$ O$_4$ Cathode Material for Lithium-Ion Batteries. *ACS Omega* **2020**, *5*, 4109−4114.

(16) Doh, C.-H.; Ha, Y.-C.; Eom, S. Entropy Measurement of a Large Format Lithium Ion Battery and Its Application to Calculate Heat Generation. *Electrochim. Acta* **2019**, *309*, 382−391.

(17) Wang, S. Entropy and Heat Generation of Lithium Cells/ Batteries. *Chin. Phys. B* **2016**, *25*, No. 010509.

(18) Jalkanen, K.; Aho, T.; Vuorilehto, K. Entropy Change Effects on the Thermal Behavior of a LiFePO$_4$/Graphite Lithium-Ion Cell at Different States of Charge. *J. Power Sources* **2013**, *243*, 354−360.

(19) Julien, C. M.; Mauger, A. NCA, NCM811, and the Route to Ni-Richer Lithium-Ion Batteries. *Energies* **2020**, *13*, No. 6363.

(20) Zhang, F.; Wu, C.; Li, K.; Deng, T. A Comparative Analysis on Thermal Stability of Delithiated Nickel-Rich NCA and NCM in Pouch Cells. *J. Electrochem. Energy Convers. Storage* **2023**, *21*, No. 011006.

(21) Kim, U.-H.; Kuo, L.-Y.; Kaghazchi, P.; Yoon, C. S.; Sun, Y.-K. Quaternary Layered Ni-Rich NCMA Cathode for Lithium-Ion Batteries. *ACS Energy Lett.* **2019**, *4*, 576−582.

(22) Zhao, S.; Yan, K.; Zhang, J.; Sun, B.; Wang, G. Reaction Mechanisms of Layered Lithium-Rich Cathode Materials for High-Energy Lithium-Ion Batteries. *Angew. Chem., Int. Ed.* **2021**, *60*, 2208−2220.

(23) Zhang, S. S. Problems and Their Origins of Ni-Rich Layered Oxide Cathode Materials. *Energy Storage Mater.* **2020**, *24*, 247−254.

(24) Chakraborty, A.; Kunnikuruvan, S.; Kumar, S.; Markovsky, B.; Aurbach, D.; Dixit, M.; Major, D. T. Layered Cathode Materials for Lithium-Ion Batteries: Review of Computational Studies on LiNi$_{1−x−y}$Co$_x$Mn$_y$O$_2$ and LiNi$_{1−x−y}$Co$_x$Al$_y$O$_2$. *Chem. Mater.* **2020**, *32*, 915−952.

(25) Zhu, H.; Huang, Y.; Ren, J.; Zhang, B.; Ke, Y.; Jen, A. K.-Y.; Zhang, Q.; Wang, X.-L.; Liu, Q. Bridging Structural Inhomogeneity to Functionality: Pair Distribution Function Methods for Functional Materials Development. *Adv. Sci.* **2021**, *8*, No. 2003534.

(26) Chen, S.-P.; Lv, D.; Chen, J.; Zhang, Y.-H.; Shi, F.-N. Review on Defects and Modification Methods of LiFePO$_4$ Cathode Material for Lithium-Ion Batteries. *Energy Fuels* **2022**, *36*, 1232−1251.

(27) Yang, X.-G.; Liu, T.; Gao, Y.; Ge, S.; Leng, Y.; Wang, D.; Wang, C.-Y. Asymmetric Temperature Modulation for Extreme Fast Charging of Lithium-Ion Batteries. *Joule* **2019**, *3*, 3002−3019.

(28) Zhu, J.; Wierzbicki, T.; Li, W. A Review of Safety-Focused Mechanical Modeling of Commercial Lithium-Ion Batteries. *J. Power Sources* **2018**, *378*, 153−168.

(29) Jiao, Y.; Hong, W.; Li, P.; Wang, L.; Chen, G. Metal-Organic Framework Derived Ni/NiO Micro-Particles with Subtle Lattice Distortions for High-Performance Electrocatalyst and Supercapacitor. *Appl. Catal., B* **2019**, *244*, 732−739.

(30) Chen, J.; Sheng, Q.; Wang, Y.; Zheng, J. Dispersed Nickel Nanoparticles on Flower-like Layered Nickel-Cobalt Double Hydroxides for Non-Enzymic Amperometric Sensing of Glucose. *Electroanalysis* **2016**, *28*, 979−984.

(31) Miller, D. J.; Proff, C.; Wen, J. G.; Abraham, D. P.; Bareño, J. Observation of Microstructural Evolution in Li Battery Cathode Oxide Particles by In Situ Electron Microscopy. *Adv. Energy Mater.* **2013**, *3*, 1098−1103.

(32) Wu, F.; Li, Q.; Chen, L.; Zhang, Q.; Wang, Z.; Lu, Y.; Bao, L.; Chen, S.; Su, Y. Improving the Structure Stability of LiNi$_{0.8}$Co$_{0.1}$Mn$_{0.1}$O$_2$ by Surface Perovskite-like La$_2$Ni$_{0.5}$Li$_{0.5}$O$_4$ Self-Assembling and Subsurface La^{3+} Doping. *ACS Appl. Mater. Interfaces* **2019**, *11*, 36751−36762.

(33) Yabuuchi, N.; Yoshii, K.; Myung, S.-T.; Nakai, I.; Komaba, S. Detailed Studies of a High-Capacity Electrode Material for Rechargeable Batteries, Li$_2$MnO$_3$−LiCo$_{1/3}$Ni$_{1/3}$Mn$_{1/3}$O$_2$. *J. Am. Chem. Soc.* **2011**, *133*, 4404−4419.

(34) Martha, S. K.; Nanda, J.; Veith, G. M.; Dudney, N. J. Electrochemical and Rate Performance Study of High-Voltage Lithium-Rich Composition: Li1.2Mn0.525Ni0.175Co0.1O2. *J. Power Sources* **2012**, *199*, 220−226.

(35) Mohanty, D.; Sefat, A. S.; Li, J.; Meisner, R. A.; Rondinone, A. J.; Payzant, E. A.; Abraham, D. P.; Wood, D. L., III; Daniel, C. Correlating Cation Ordering and Voltage Fade in a Lithium−Manganese-Rich Lithium-Ion Battery Cathode Oxide: A Joint Magnetic Susceptibility and TEM Study. *Phys. Chem. Chem. Phys.* **2013**, *15*, No. 19496.

(36) Li, Z.-Y.; Guo, H.; Ma, X.; Sun, K.; Chen, D.; He, L.; Han, S. Al Substitution Induced Differences in Materials Structure and Electro-chemical Performance of Ni-Rich Layered Cathodes for Lithium-Ion Batteries. *J. Phys. Chem. C* **2019**, *123*, 19298−19306.

(37) Li, J.; Harlow, J.; Stakheiko, N.; Zhang, N.; Paulsen, J.; Dahn, J. Dependence of Cell Failure on Cut-Off Voltage Ranges and Observation of Kinetic Hindrance in LiNi$_{0.8}$Co$_{0.15}$Al$_{0.05}$O$_2$. *J. Electrochem. Soc.* **2018**, *165*, A2682−A2695.